

MEASURING GALAXY CLUSTERING AND THE EVOLUTION OF [CII] MEAN INTENSITY WITH FAR-IR LINE INTENSITY MAPPING DURING $0.5 < z < 1.5$

B. D. UZGIL^{1,2}, J. E. AGUIRRE¹, AND C. M. BRADFORD²

Draft version May 5, 2014

ABSTRACT

We explore the possibility of studying the redshifted [CII] fine structure transition through cosmic time using the three-dimensional (3D) power spectra obtained with an imaging spectrometer. The intensity mapping approach measures the spatio-spectral fluctuations due to line emission from all galaxies, including those below the individual detection threshold. This technique not only provides 3D measurements of galaxy clustering, but contains astrophysical information—namely, the average intensity of total [CII] emission—which can be extracted from the linear portion of the power spectrum, with redshift information naturally encoded. We further compare the intensity mapping approach to galaxy surveys comprised of individually detected galaxies, and find that intensity mapping provides an unbiased estimate of the mean [CII] intensity. Depending on the noise level of a given experiment, intensity mapping may provide the only means of measuring this aggregate quantity. Also, depending on the shape of the luminosity function, intensity mapping can be a more efficient means of measuring the power spectrum.

Keywords: far-infrared spectroscopy; galaxy redshift surveys

1. INTRODUCTION

Various observational techniques in astronomy, including, but not limited to, photometric and spectroscopic stacking analysis, $P(D)$ fluctuation analysis, and recently, cosmological spectral deconvolution (cf. Dole et al. (2006); Glenn et al. (2010); de Putter et al. (2014) for examples of each), have been developed to provide a means to study the nature of galaxies that are otherwise too faint to be detected individually at high significance. These methods rely heavily on interpreting the statistical and aggregate properties of the extragalactic sources, and yet the insight they have provided into the nature of galaxies and their evolution with cosmic time has been invaluable.

Line intensity mapping, or 3-D tomographic mapping, is another technique that allows astronomers to probe extragalactic light from all sources, including the faintest galaxies and even diffuse intergalactic emission. An intensity mapping survey of a spectral line at different frequencies *produces a fully three dimensional data cube containing “tomographic scans” of the Universe along the spectral (i.e., redshift) direction*. The spatial fluctuations in line emission, contained in the data cube, are then decomposed into the power spectrum. Atomic (Gong et al. 2012; Visbal et al. 2011) and molecular (Lidz et al. 2011; Gong et al. 2011) transitions – such as the 21-cm spin flip transition from H^o, CO (2-1), and [CII] 158 μ m – have been investigated as candidates for intensity mapping experiments during the Epoch of Reionization (EoR). Of these, the neutral hydrogen case is undoubtedly the most developed in terms of its standing in the literature (cf. Morales & Wyithe (2010) for a review) and in the experimental arena (e.g., PAPER (Parsons et al. 2013), MWA (Tingay et al. 2013)) because intensity mapping is the only means of studying the intergalactic HI light.

[CII] later emerged as an EoR intensity mapping candidate since it both offers a way to probe the faint end of the luminosity function, and provides an opportunity for cross correlation with the HI datasets (Gong et al. 2012).

Experiments targeting lower redshifts can offer a proof of principle of the approach, and neutral hydrogen is also the most mature in this respect. At $z \sim 0.8$, Chang et al. (2010) measured the cross correlation between the 21-cm emission and a galaxy catalog and Switzer et al. (2013) put limits on the 21cm auto-power. Pullen et al. (2013) explored the feasibility of measuring the clustering in Lyman alpha emission from the EoR and down to $z \sim 2$.

Here we examine the application of the intensity mapping technique to moderate redshifts, targeting the fine structure line emission from ionized carbon during $0.5 < z < 1.5$. The majority of extragalactic [CII] arises from the neutral and ionized interstellar medium (ISM) of star-forming galaxies, with only a negligible contribution from the IGM (Gong et al. 2012). This far-infrared (FIR) line is a well-suited probe of the galaxy population during the relevant time frame, as the mean dust attenuation in galaxies peaks at $z \sim 1.5$, when roughly 80% of the cosmic star formation rate density is obscured and captured only in the infrared emission of re-processed starlight by dust grains (Burgarella et al. 2013). Moreover, [CII] is typically the brightest FIR line emitted from the ISM of galaxies, with luminosities up to 0.1% of the IR luminosity, and is an important sign-post of star formation and related dynamics in galaxies (Graciá-Carpio et al. 2011; Sargsyan et al. 2012; Díaz-Santos et al. 2013).

A power spectrum analysis of 3-D [CII] tomography expands upon recent works that utilize the fluctuations in emission rather than individual object detections to study the properties of dusty, star-forming galaxies (DSFGs). (See Casey et al. (2014) et al for a review of DSFGs at the redshifts of interest to this study.) These studies, using $P(D)$ (Glenn et al. 2010; Béthermin et al. 2011) or

badeu@sas.upenn.edu

¹ University of Pennsylvania, Philadelphia, PA 19104

² Jet Propulsion Laboratory

a 2-D power spectrum (Viero et al. 2012) analysis, have already shed light on some aspects (such as the number counts or spatial clustering) of the bulk of these systems from $z = 1 - 3$, but they are limited by source confusion or uncertainties associated with the lack of redshift information, respectively. Redshift ambiguities can be removed to some extent with galaxy-by-galaxy surveys with the interferometers ALMA or NOEMA, or with an instrument like X-Spec, a proposed multi-object spectrometer for CCAT. However, the interferometer surveys will be expensive, and the CCAT surveys, though faster, will not reach the faintest galaxies in the luminosity function. Power spectrum treatment of the 3-D maps naturally combines the redshift precision of spectral measurements, while including all sources in the luminosity function, and can be carried out with an instrument that does not require exquisite point-source sensitivity.

This sensitivity of the power spectrum to galaxies below the individual detection threshold, indeed to the mean aggregate intensity in the line from all sources, is a unique line of inquiry for the galaxy populations. Namely, by extracting the mean intensity of [CII], or any emission line of interest, from the power spectrum at a number of observed frequencies, intensity mapping provides a means of quantifying the aggregate luminosity from all [CII]-emitting sources at a given redshift. An example of using the power spectrum to determine luminosity density can be found in Planck Collaboration et al. (2013), although the results discussed there were derived from the 2-D angular power spectrum of IR continuum fluctuations, which relies on fits which include uncertainties in the dust spectral energy distributions, for instance. With inherent redshift information from the spectral line, such an observation of the 3-D power spectrum would ascertain the cosmic evolution of the Universe's total output in [CII] with a level of precision not available by other means.

The organization of this paper is as follows. We have calculated the mean intensity for a suite of fine structure IR emission lines, including the [CII] line, based on the IR luminosity function and empirical line-to-IR luminosity correlations, and present these results in the context of a power spectrum model in Section 2. In Section 3, we envision a suitable platform—namely, a balloon-borne experiment operating at frequencies between $240\mu\text{m}$ to $420\mu\text{m}$ —for conducting the [CII] intensity mapping experiment and discuss the feasibility of detecting the [CII] power spectra in terms of the Signal-to-Noise Ratio. From the power spectra, we provide estimates for accuracy on measuring the mean [CII] intensity as a function of redshift. To better assess the value of intensity mapping studies in the case of [CII] at moderate redshifts, and of intensity mapping experiments in general, we compare in Section 4 the performance of the intensity mapping approach against spectroscopic galaxy surveys that rely on individual detections of sources to measure the power spectrum. In particular, we examine the effects of variations in luminosity function shape, aperture diameter (and, consequently, pixel size), and experimental noise on the ability of each observational method to measure the power spectrum and provide a complete view of the galaxy population.

2. PREDICTIONS FOR FIR LINE POWER SPECTRA

2.1. Relationship Between Galaxy Populations and Fluctuation Power

The complete auto power spectrum of a given FIR line as a function of wavenumber k , $P_{i,i}(k, z)$, can be separated into power from the clustering of galaxies, $P_{i,i}^{clust}(k, z)$ and a Poisson term describing their discrete nature, $P_{i,i}^{shot}(z)$. We compute the full nonlinear matter power spectrum, $P_{\delta,\delta}(k, z)$, using the publicly available code HALOFIT+ (<http://camb.info>), which has been the standard tool for predicting matter power spectra upon its success in fitting state-of-the-art dark matter simulations over a decade ago (Smith et al. 2003). The clustering component of the line power spectrum is then written as

$$P_{i,i}^{clust}(k, z) = \bar{S}_i^2(z) \bar{b}_i^2(z) P_{\delta,\delta}(k, z). \quad (1)$$

Here we have implicitly assumed that the fluctuations in line emission trace the matter power spectrum with some average bias, $\bar{b}_i(z)$, chosen in line with observations of galaxies from the redshift range of interest to this study (Cooray et al. 2010; Jullo et al. 2012). By assuming a bias, it should be noted that our model does not take into account a possibly variation of the source bias with the host halo mass (and thus luminosity), but XXX

The mean line intensity, $\bar{S}_i(z)$, in units of Jy sr^{-1} , can be calculated as

$$\bar{S}_i(z) = \int dn_i \frac{L_i}{4\pi D_L^2} y_i D_A^2, \quad (2)$$

where the integration is taken with respect to n_i , the number of galactic line emitters per cosmological comoving volume element. (The factor y_i is the derivative of the comoving radial distance with respect to the observed frequency, i.e. $y = d\chi/d\nu = \lambda_{i,rest}(1+z)^2/H(z)$, and D_A is the comoving angular distance.)

Finally, the shot noise component of the total line power spectrum—with the same units as the clustering term, namely, $\text{Jy}^2 \text{sr}^{-2} (\text{Mpc h}^{-1})^3$ —takes the form

$$P_{i,i}^{shot}(z) = \int dn_i \left(\frac{L_i}{4\pi D_L^2} \right)^2 (y_i D_A^2)^2. \quad (3)$$

2.2. Calculating IR line volume emissivity

The number density of line emitters and the line luminosity that appear in Equations 2 and 3 can be derived by a variety of methods. In earlier papers on intensity mapping of molecular and fine-structure emission lines at high redshift ($z \gtrsim 6$), one approach involved using the dark matter halo mass function in lieu of the line emitter density (and invoking a one-to-one correlation between halos and galaxies, which is reasonable at high redshifts). The line luminosity, in turn, could be scaled according to the star formation rate, which was related to halo mass via a proportionality constant comprised of factors describing the fraction of baryons available for star formation, as well as the dynamical timescale for star formation and a duty cycle for emission. While this approach is perhaps justified for the very early Universe (given the lack of information about the galaxy luminosity function at high redshift), the situation at later times is better

understood; we make use of empirical constraints on the $z \sim 1$ epoch from FIR/submm number counts and observations of FIR line emission in galaxies.

We first employ the empirically-constrained, backwards-evolution model of the IR luminosity function $\Phi(L_{IR}, z)$ from Béthermin et al. (2011) (hereafter B11) to predict the number of galaxies with luminosity L_{IR} at a given redshift in some comoving volume of the Universe per logarithmic luminosity interval, i.e., $\frac{dN(L_{IR}, z)}{dV d\log_{10} L_{IR}}$ or $\frac{dn_{IR}}{d\log_{10} L_{IR}}$.

To convert the infrared luminosity to a line luminosity, we apply the relation for L_i as a function of L_{IR} provided by Spinoglio et al. (2012). The fit in their paper was based on the collection of ISO-LWS observations of local galaxies in Brauer et al. (2008). For example, we reproduce below the relation for [CII]

$$\log_{10} L_{[CII]} = (0.89 \pm 0.03) \log_{10} L_{IR} - (2.44 \pm 0.07), \quad (4)$$

indicating that [CII] is suppressed for higher luminosity systems. The choice of using local L_i - L_{IR} relations for our study of $z \sim 1$ emitters may be unrealistic due to findings that suggest the so-called “deficit” in [CII] and other FIR lines evolves with redshift such that the high- z counterparts to local systems do not exhibit suppressed FIR line emission. The local IR relations should then be viewed as a lower limit in estimating the emission of the fine structure lines, since we likely overestimate the deficiency in the high luminosity systems of our model. While in Section XXX we explore variations in the shape of the IR luminosity function and consider an alternative line-to-IR luminosity ratio, we use the combined Béthermin-Spinoglio model to predict line intensities and adopt it as our fiducial model throughout this paper.

Next, it becomes possible to write the cosmic mean intensity and shot noise of the line, in units of Jy sr^{-1} , as a function of redshift based on the B11 luminosity function and Spinoglio et al. (2012) $L_i - L_{IR}$ relation as

$$\bar{S}_i(z) = \int_{L_{IR, min}}^{L_{IR, max}} d\log L_{IR} \Phi(L_{IR}, z) \frac{f_i L_{IR}}{4\pi D_L^2} y D_A^2 \quad (5)$$

$$P_{i,i}^{shot}(z) = \int_{L_{IR, min}}^{L_{IR, max}} d\log L_{IR} \Phi(L_{IR}, z) \left(\frac{f_i L_{IR}}{4\pi D_L^2} y D_A^2 \right)^2 \quad (6)$$

where f_i , i.e. $\frac{L_i(L_{IR})}{L_{IR}}$, is the fraction of IR luminosity emitted in line i , as computed from equation (3). In other words, we have written \bar{S}_i and $P_{i,i}^{shot}(z)$ as the first and the second moments of the luminosity function.

The resulting mean intensities for a variety of FIR lines are plotted in Figure 1 as a function of redshift and observed wavelength. \bar{S}_i vs λ_{obs} can be interpreted as identifying the dominant source of fluctuations, according to our model, for a given frequency. As a specific example, if the target line of an observation is [OI]63 μm at $z = 1$, it is necessary to distinguish between the target line and interlopers like [OIII]88 μm from $z = 0.4$ and [OIII]52 μm from $z = 1.4$, which contribute power at the observed frequency. Visbal & Loeb (2010) showed how the cross spectra can be used to differentiate between a

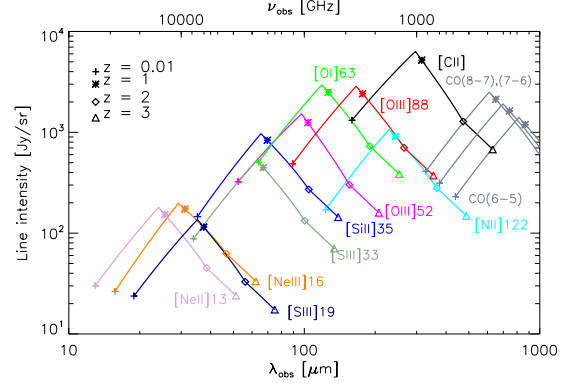


Figure 1. : Intensity of fine structure line emission as a function of observed wavelength for the empirical model based on the B11 luminosity function.

target line and a contaminating line (or “bad line”, in their words), since emitters at different redshifts will be spatially uncorrelated. For the observed wavelengths of [CII], however, it is apparent from Figure 2 that, with the exception of contributions from [OIII]88 μm and CO(8-7) near [CII] at $z \sim 0.01$ and $z > 2$, respectively, the [CII] line is relatively unaffected by interloper lines—a result of its luminosity and spectral isolation. From a purely practical perspective, then, [CII] at $z \sim 1$ is a favorable target for line intensity mapping.

3. OBSERVATIONAL STRATEGY: COMPARING INTENSITY MAPPING WITH TRADITIONAL GALAXY SURVEYS

Now let us turn to a question regarding the motivation for intensity mapping in general, as well as in the specific case of [CII] at the redshifts relevant to this study. Having identified the galaxy redshift surveys as an alternative method to measure the 3D clustering power spectrum, it is natural to consider the relative merits of the two approaches.

The principal advantage of intensity mapping is that it naturally measures the mean intensity per equation 5, regardless of the shape of the luminosity function. Galaxy surveys always miss some of the light in the faintest galaxies, and this completeness problem is illustrated in Figure 5. To make concrete comparisons in what follows we employ toy models for the infrared luminosity function (Figure 4 written in the Schechter formalism—parametrized by the usual α , L_* , and ϕ_* —and normalize the total luminosity density to the empirical model from Section 2 (cf. Appendix for details). We stress that these Schechter models are not intended to represent a real interpretation of the distribution of galaxies, but are merely helpful for illustrating the effect of the LF *shape* on the relative usefulness of intensity mapping and traditional galaxy surveys.

The line sensitivity, S_γ (units of $\text{W m}^{-2} \text{s}^{1/2}$), is the figure of merit for detecting an unresolved line in a point source, and we define individual detections at the 5σ level as having a flux above the instrumental noise in a pixel, i.e., above $5 \times S_\gamma t_{pix}^{-1/2}$. (For this analysis, we have assumed the galaxy surveys have reliable spectroscopic redshifts and thus neglect the problem of confusion noise.)

Since the intensity mapping technique contains information in the power spectrum from sources below a given

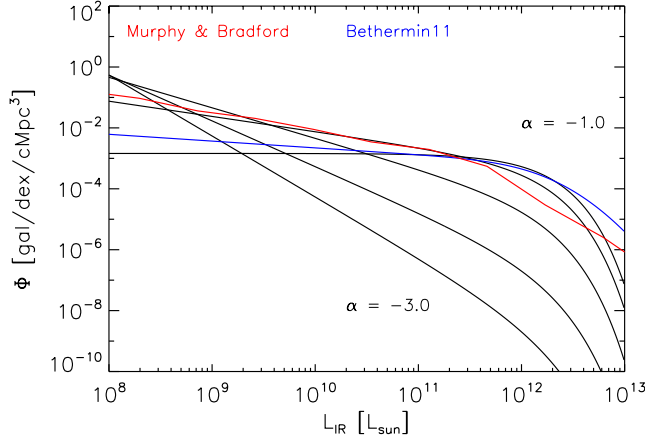


Figure 2. : Toy model IR luminosity functions with faint-end slope (from top to bottom) $\alpha = -1.0, -1.5, -2.0, -2.5, -3.0$. The B11 and Murphy & Bradford models are plotted as blue and red curves, respectively, for comparison.

S_γ , we expect that regimes in which the majority of galaxies are too faint to be resolved are better-suited for intensity mapping observations than observations via the traditional galaxy survey.

One such regime is when the bulk of the galaxy number density at a certain redshift is comprised of galaxies with sub- L_* luminosities (i.e., for steep slope α in the LF). This case is illustrated in the middle and righthand panels in the bottom row of Figure 5, where, for LFs with α of -1.5 or -2.0, the galaxy surveys detect only 40% and 3% of the total [CII] light in integrating to an f_{err} of 10. The top row of this figure breaks down the total emission in terms of the number of detectable galaxies. As is clear from comparison of panels in the top and bottom rows, a large sample of galaxies (of order 1,000 or greater) does not necessarily ensure an unbiased measure of the mean [CII] intensity; one must take into account the experimental fractional error, as well as the faint-end slope. If, however, one extracts the aggregate, unresolved emission from [CII] via the intensity mapped power spectrum, one is essentially measuring $\frac{\rho_{[CII],obs}}{\rho_{[CII]}} = 1$ as soon as SNR on the linear clustering term of the power spectrum is sufficiently high, which we depict in Figure 10.

There may be applications for which the mean intensity is not required, and the shape of the power spectrum, rather than its absolute value, is of interest. For this application, we compare the SNR on a k bin for both galaxy detection and intensity mapping surveys (denoted, respectively, by the subscripts “GS” and “IM”), with the expressions:

$$SNR_{GS} = \frac{\sqrt{N_{modes}}}{1 + 1/(b_i^2 P_{\delta,\delta} \bar{n}_{gal})} \quad (7)$$

$$SNR_{IM} = \frac{\sqrt{N_{modes}}}{1 + P_N / (\bar{S}_i^2 b_i^2 P_{\delta,\delta})} \quad (8)$$

Even in this limited comparison of relative SNRs, the intensity mapping often outperforms galaxy surveys, as shown in Figure 6. In this figure, for the fiducial aperture

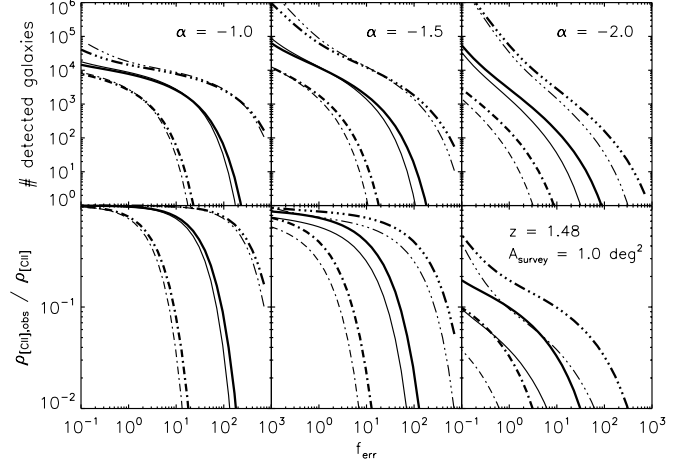


Figure 3. : The predicted number of [CII]-detected galaxies and observed fraction of [CII] luminosity density as a function of survey time for the square degree field. Solid curves correspond to the fiducial aperture, $d_{ap} = 2.5$ m. Dashed curves correspond to apertures scaled by a factor $\sqrt{\epsilon}$, where $\epsilon = 0.1$ (triple-dot-dashed) and $\epsilon = 10.0$. Thin curves correspond to our fiducial model for [CII] line intensity, based on Spinoglio fits, whereas thick curves denote the use of a constant ratio of $\frac{L_{[CII]}}{L_{IR}} = 10^{-3}$.

(solid curves), the intensity mapping method (magenta curve) has higher SNR than the corresponding galaxy survey for all fractional errors. (Note the galaxy survey and intensity mapping survey map identical fiducial areas in this example.) However, for the flattest faint-end slope ($\alpha = -1$, lefthand panel), $SNR_{GS} > SNR_{IM}$ for $20 < f_{err} < 100$. We point out that $SNR_{IM} > SNR_{GS}$ for very high and very low f_{err} in the case of $\alpha = -1.0$, which correspond to shot-noise dominated and cosmic variance-dominated regimes, respectively, for the galaxy surveys. It is important to note, while surveys may detect a large number of galaxies, and thus SNR_{GS} on the power spectrum may be appreciable, the power spectrum of detected galaxies may not yield a measurement of mean intensity, for which a large fraction of the total [CII] light must be observed (cf. Figure ??ngal $_{frac}$).

Figure 6 also shows the effect of changing pixel area by a factor ϵ —due to a change in the telescope’s aperture diameter by $\epsilon^{-1/2}$ —on the SNR. Because the area of the survey is fixed, the transformation on pixel area leads to a change in S_γ by the same factor ϵ , but will not alter P_N (as seen previously in Eq. 12) for the intensity mapping experiment; SNR_{IM} of large-scale clustering modes is robust to changes in pixel area. Thus, the instruments with smaller pixels (triple-dot dashed curve, $\epsilon = 0.1$) achieve greater depths than their large pixel counterparts (dot-dashed curve, $\epsilon = 10.0$), and thus attain higher SNR by resolving more galaxies. Meanwhile, galaxy surveys with large pixels find themselves in the disabling condition of having many sources that are below the detection threshold in a single voxel. Whether or not the galaxy survey experiments with small pixel area outperform the intensity mapping experiment is, however, dependent on the faint-end slope of the luminosity function.

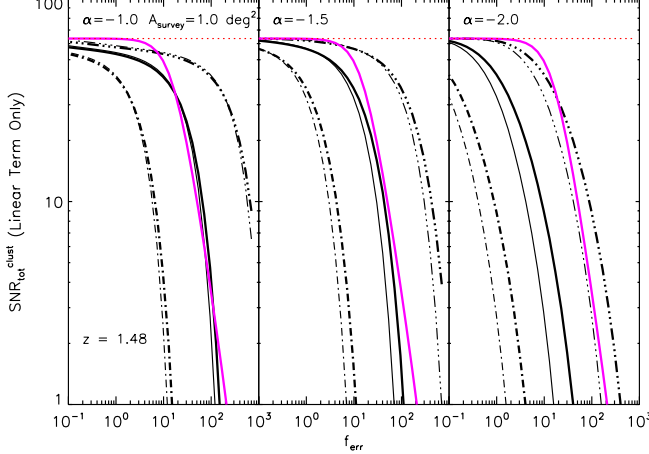


Figure 4 : Total Signal-to-Noise ratio on the linear portion of the clustering power spectrum of [CII] at $z = 1.48$ as a function of the fractional error. SNR_{IM} and SNR_{GS} are plotted as the magenta and black curves, respectively. Solid curves correspond to the fiducial aperture, $d_{ap} = 2.5$ m. Dashed curves correspond to apertures scaled by a factor $\sqrt{\epsilon}$, where $\epsilon = 0.1$ (triple-dot-dashed) and $\epsilon = 10.0$. The horizontal dotted red line is the maximum SNR possible, set by the number of modes in the survey volume. Thin curves correspond to our fiducial model for [CII] line intensity, based on Spinoglio fits, whereas thick curves denote the use of a constant ratio of $\frac{L_{[CII]}}{L_{IR}} = 10^{-3}$.

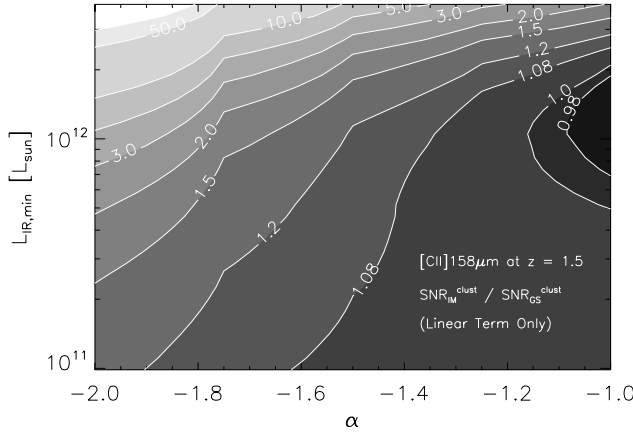


Figure 5 : Contours of SNR_{IM}/SNR_{GS} for the linear term in the [CII] clustering power spectrum at $z = 1.5$, determined for a given depth (in L_{IR}) and IR LF faint-end slope α .

3.1. [CII] Luminosity Functions and Expected Power Spectra

As laid out in Equation 1, $P_{[CII],[CII]}^{clust}$ is sensitive to intensity fluctuations from the full range of normal ($L_{IR} < 10^{11} L_{\odot}$) to ULIRG-class ($L_{IR} > 10^{12} L_{\odot}$) systems because its amplitude is proportional to the mean line intensity, squared. The information contained in a power spectrum constructed from a survey of individually de-

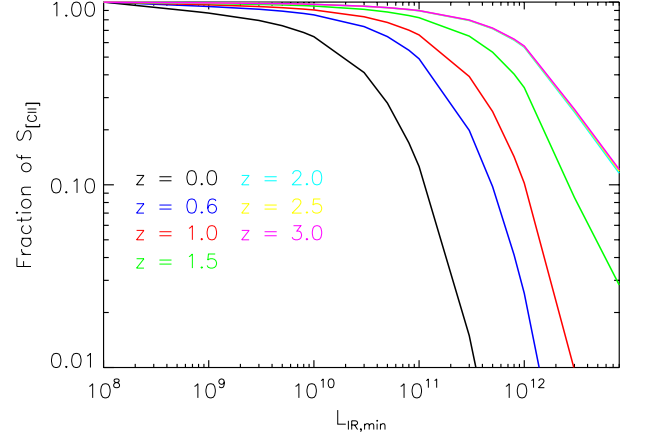


Figure 6 : The fraction of total [CII] mean intensity as a function of lower limit in the luminosity function. Different color curves represent different redshifts, as labeled on the plot.

tected galaxies is, in contrast to the line intensity mapping approach, necessarily limited to galaxies which are above a certain detection threshold, or $L_{IR,min}$. Figure 2 shows the integrated luminosity functions for [CII] in our model, which gives a sense of the depth that a galaxy survey must reach in order to completely probe the full integrated [CII] emission, i.e. all of \bar{S}_i . In this section, we examine the role of the various luminosity ranges on the amplitude of the observed [CII] power.

Power spectra at four representative redshifts ($z = 0.63, 0.88, 1.16$, and 1.48) comprised of the sources above a few different survey depths are represented by Figure 3. (Note that we use $\Delta_{[CII],[CII]}^2 = k^3 P_{[CII],[CII]}(k)/(2\pi^2)$ when plotting the power spectrum. In this notation, the factor k^3 cancels out the volumetric units of $P_{\delta,\delta}(k, z)$ and the integral of $\Delta_{[CII],[CII]}^2$ over logarithmic k bins is equal to the variance in real space.) At these redshifts, respectively, the average linear bias has been assumed to be $\bar{b} = 2.0, 2.3, 2.6$, and 2.9 . In this Figure, we see the clustering amplitude decrease as the IR detection threshold is raised from $10^8 L_{\odot}$ to $10^{12} L_{\odot}$. (Note that the reduction in the clustering amplitude is precisely the square of the factor of reduction in $\bar{S}_{[CII]}$ plotted in Figure 2.) The level of decrease in clustering power as a result of raising $L_{IR,min}$ is most dramatic at the lower end of the redshift range of interest, when the luminosity function is represented mostly by normal galaxies and LIRGs. As ULIRGs rise to dominate the IR luminosity function at $z = 1.48$, we see that the amplitude of the clustering component of $P_{[CII],[CII]}(k, z)$ at this redshift is relatively robust until $L_{IR,min} \sim 10^{11} L_{\odot}$, implying that a large fraction of the fluctuations are captured at this depth; we infer from Figure 2 that, at $z = 1.48$, individually resolving galaxies at a depth of $6 \times 10^{11} L_{\odot}$ will recover half of the [CII] light, at which point the residual power of unresolved galaxies is a quarter of the total predicted power. (In our model, one estimates the power of unresolved galaxies as the factor $(1 - x)^2$, where x is the fraction of observed light.) For redshifts $z = 0.63, 1.16$ and 3.0 , the corresponding depths to ob-

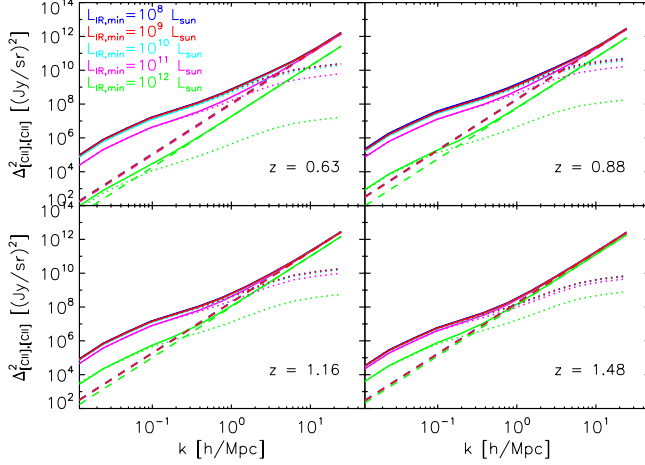


Figure 7. : Predicted [CII] power spectra from $z = 0.63$ to $z = 1.48$. Blue, red, cyan, magenta, and green curves represent the power spectrum computed with a lower limit in the luminosity function corresponding to 10^8 , 10^9 , 10^{10} , 10^{11} , and $10^{12} L_\odot$, respectively.

serve half of the [CII] light are $\sim 10^{11}$, 2×10^{11} , and $10^{12} L_\odot$, respectively. For reference, state-of-the-art instruments aboard future space telescopes will reach 5σ -1hr line sensitivities down to a few times $10^{-19} \text{ W m}^{-2}$, corresponding to $L_{IR,min} \sim 10^{12} L_\odot$ at $z = 1.5$.

4. THE [CII] POWER SPECTRUM

4.1. Observational Sensitivity to the Power Spectrum

We present in this section predictions for the [CII] power spectrum with error bar estimates for a feasible experimental platform, namely, a balloon-borne experiment that allows for uninterrupted spectral coverage in the wavelength range 240 to 420 μm pertinent to this study. Fiducial experimental parameters are summarized in Table 1. The telescope mirror aperture, D_{ap} , survey area, A_{survey} , and total observing time, t_{obs}^{survey} , are taken as 2.5 m, 1 deg^2 , and 200 hours, respectively, though we explore the effect of varying D_{ap} and A_{survey} on SNR (cf. Figure 9).

Error bar estimates and the total SNR for the power spectrum are calculated by assuming a spectrally flat noise power spectrum, so that the noise power in each pixel, P_N , is written as

$$P_N = \sigma_N^2 \frac{V_{pix}}{t_{pix}}, \quad (9)$$

where σ_N^2 is the instrument sensitivity (noise equivalent intensity, or NEI, in units of $\text{Jy sr}^{-1} \text{s}^{1/2}$), V_{pix} is the volume of a pixel, and t_{obs}^{pix} is the time spent observing on a single pixel. The variance of a measured k , $\sigma^2(k)$, is then written as

$$\sigma^2(k) = \frac{(P_{[CII],[CII]}(k) + P_N(k))^2}{N_{modes}}, \quad (10)$$

where N_{modes} is the number of wavemodes that are sampled for a given k bin of some finite width $\Delta \log(k)$. (We have chosen $\Delta \log(k) = 0.3$ for this analysis.)

The total SNR, in turn, is calculated from the expression

$$SNR_{tot} = \sqrt{\sum_{bins} \left(\frac{P_{[CII],[CII]}(k)}{\sigma(k)} \right)^2} \quad (11)$$

The expected [CII] power spectrum, with corresponding predictions for SNR, at the same redshifts from Figure 3 are shown in Figure 8. In calculating the power spectrum sensitivity for these power spectra, the two lowest line-of-sight modes and the lowest transverse mode are not included, since these modes will likely be compromised by the necessity of continuum foreground subtraction and beam-differencing in the fluctuation analysis. (The exact effect of continuum subtraction will need to be modeled via simulation.) We find that the total power spectrum, including power from both shot noise and clustering, is observable with $SNR > 10$ in the redshift range from $z = 0.88 - 1.48$; the clustering power, in turn, can be detected with $SNR > 5$ at all examined redshifts.

In Figure 9 we examine the effect on SNR of changing the survey area and telescope aperture, where the SNR has been plotted as a function of k . To better demonstrate how the observational parameters drive the behavior of $SNR(k)$ illustrated in this Figure, we rewrite P_N in terms of the parameters from Table 1, giving

$$\begin{aligned} P_N &= \left(\sigma_N^2 A_{pix} \Delta r_{los}^{pix} \right) / \left(\frac{t_{survey}}{n_{beams}/N_{instr}^{spatial}} \right) \\ &= \left(\sigma_N^2 A_{pix} \Delta r_{los}^{pix} \right) / \left(\frac{t_{survey} N_{instr}^{spatial}}{A_{survey}/A_{pix}} \right) \\ &= \sigma_N^2 \frac{\Delta r_{los}^{pix} A_{survey}}{t_{survey} N_{instr}^{spatial}} \end{aligned} \quad (12)$$

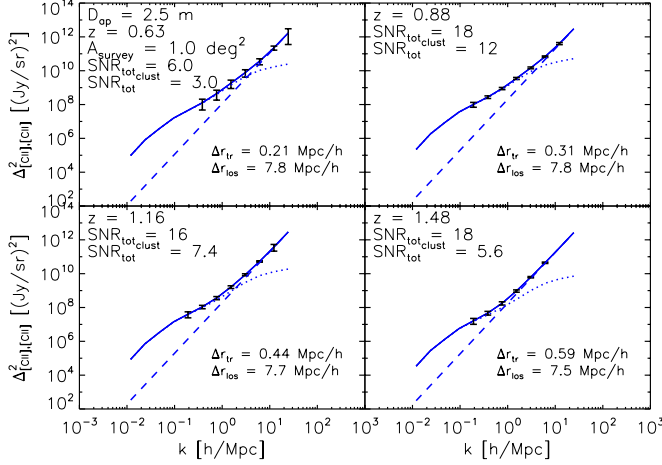
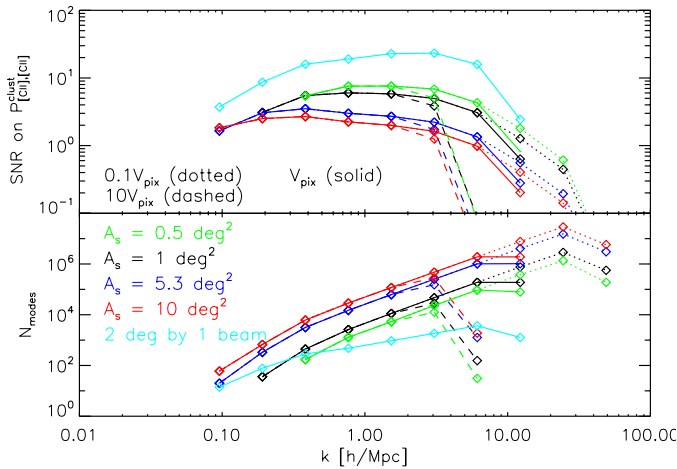
In this form, it becomes apparent that—with fixed number of spatial pixels, spectral resolution, and total observing time—the only factor driving up the amplitude of noise power is the survey area; the effect of increasing aperture only allows access to higher wavenumbers, which can be useful for subtracting the shot noise from the total power in later steps of data analysis.

4.2. Measuring $\bar{S}_{[CII]}(z)$

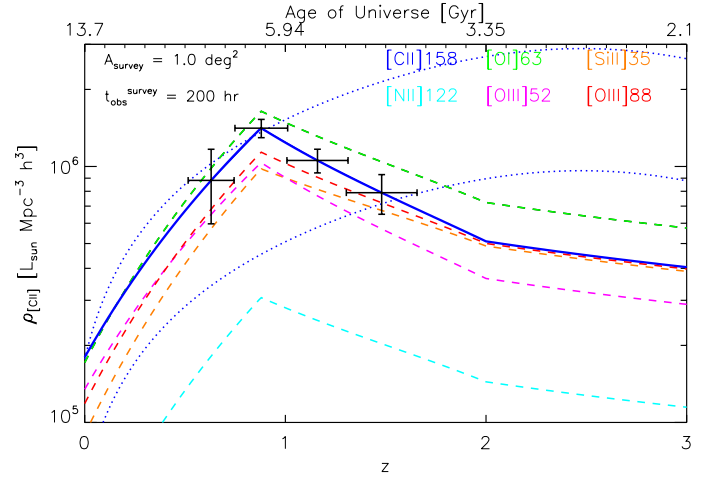
As noted above, intensity mapping is naturally sensitive to the full range of galaxy luminosities through the mean intensity, which is imprinted in the linear (2-halo) clustering term. Shot noise must be accurately subtracted, and this should be straightforward given the high SNR in the shot-noise dominated k bins (Figure 9). Next, per Equation 1, it is necessary to divide out $P_{\delta,\delta}(k, z)$ and $\bar{b}_{[CII]}^2(z)$. The confidence with which a *a priori* known quantities becomes lower as k increases. For example, the 1-halo power spectrum for DSFGs appears to be dependent on the IR luminosity of the contributing sources (Viero et al. 2012), indicating the need to map sufficiently wide areas that access k modes where the power is largely independent of the level of 1-halo power.

Table 1: Fiducial Parameters for Envisioned Balloon Experiment

$R = \nu_{obs}/\delta\nu$	450			
t_{obs}^{survey} (hr)	200			
D_{ap} (m)	2.5			
A_{survey} (deg ²)	1.0			
z	0.63	0.88	1.16	1.48
$\bar{S}_{[CII]}$ (Jy sr ⁻¹)	4.56×10^3	6.33×10^3	4.05×10^3	2.55×10^3
NEI (10 ⁷ Jy sr ⁻¹ sec ^{1/2})	3.4	2.1	1.5	1.0
Line Sensitivity (10 ⁻¹⁷ W m ⁻² sec ^{1/2})	1.58	1.13	0.92	0.71
Wavelength Range (μm)	240-276	276-317	317-365	365 - 420
$\delta\nu$ (GHz)	2.58	2.25	1.95	1.70

**Figure 8 :** Predicted [CII] power spectra with error bar estimates from $z = 0.63$ to $z = 1.48$ for telescope with 2.5 meter aperture and a survey area of 1 square degree, and with a total observing time of 200 hours. Dotted curves indicate power from clustering (including contributions from linear and nonlinear terms), and dashed curves indicate the contribution from shot noise power.**Figure 9 :** Signal-to-noise on the clustering term of the [CII] power spectrum $P_{[CII]}^{clust}$ and number of modes as a function of k at $z = 0.88$. The black, blue, and red lines correspond to survey areas of 1.0, 5.3, and 10.0 deg², respectively. Telescopes with apertures yielding 0.1, 1, and 10 times the fiducial pixel volume, V_{pix} , are shown as the dotted, solid, and dashed lines, respectively.

Returning to Figure 9, we see that, for the purpose of measuring $\bar{S}_{[CII]}$ with the fiducial survey of 1 deg², there are two k bins ($k = 0.16$ and 0.27 h/Mpc) in which the 2-halo clustering accounts for at least 75% of the total power. (Surveys with $A_{survey} = 5.3$ and 10 deg², also shown in Figure 9, are wide enough to have three k bins available in the linear regime, but the sensitivity on the additional mode with $t_{obs}^{survey} = 200$ hours is marginal.) Thus, in considering the case of $A_{survey} = 1.0$ deg², we find that it is possible to measure $\rho_{[CII]}(z)$ within $\sim 10\%$ accuracy from $z = 0.63$ to $z = 1.48$, as shown in Figure 10, where the fractional uncertainty on $\bar{S}_{[CII]}(k, z)$ has been calculated as half the fractional uncertainty on $P_{[CII],[CII]}(k, z)$. In Figure 10, we also include, for comparison, an estimate for $\rho_{[CII]}(z)$ based on the analytic fit to SFRD(z) provided by Hopkins & Beacom (2006) and a constant ratio of 0.003 between $L_{[CII]}$ and L_{IR} . (We use the correlation between SFRD and infrared luminosity described in Kennicutt (1998).)

**Figure 10 :** Error bar estimates on $\rho_{[CII]}$, as measured by the fiducial experiment, at observed redshifts $z = 0.63$, 0.88 , 1.16 , and 1.48 . Errors in z correspond to the redshift space spanned by the spectrometer bandwidth. The solid blue curve is the underlying model for [CII] mean intensity. The luminosity density of other bright IR lines are shown as the dashed colored curves, and the dotted curve is an estimate for $\rho_{[CII]}$ based on the fit to SFRD(z) provided by Hopkins & Beacom (2006) and a constant ratio of $L_{[CII]}$ to L_{IR} equal to 0.003.

5. INSTRUMENT CAPABILITIES

[Table of f_{err} -to-instrument conversion for the balloon and space telescope goes here.]

6. SUMMARY AND OUTLOOK

[under construction: MB Apr 22: The first sentence should be more general that CII – it should talk about intensity mapping in general. Note the mean intensity, and the fact that, even mean intensity aside, the the SNR is higher in cases of small apertures and/or steep faint end luminosity function slope. Then you can have a few sentences about reionization (your current section 5), but I suggest removing 'indeed' and 'Not to mention,' and if there are any other references on the faint end slopes I would add them.]

As noted in Section 4, galaxy surveys performed using instruments with small telescopes and large pixels fare worse in the detection of individual galaxies, and, hence, in measuring the power spectrum compared to intensity mapping experiments using an identical instrument. Another regime where galaxy surveys find themselves in the large-pixel limit is at high-redshift, and so the early studies of [CII] intensity mapping during Reionization are, indeed, well-motivated in this regard. Not to mention, there is also strong evidence for steep ($\alpha \sim -2$) luminosity functions in the rest frame UV at $z \sim 7$ (Bouwens et al. 2014), which additionally positions intensity mapping experiments as better-suited probes of the power spectrum and the aggregate galaxy population than galaxy redshift surveys. Although beyond the scope

of this paper, our findings here reinforce the notion that the $z > 6$ Universe presents an ideal opportunity to learn about galaxy populations via intensity mapping

should mention also future NASA FIR surveyor missions (SAFIR?)

We have presented predictions for the measurement of the [CII] power spectrum between $0.63 < z < 1.48$, and demonstrated the detectability of the power spectrum in both clustering and shot noise terms in this redshift range. Fluctuations of [CII] intensity have been modeled by combining empirically-constrained estimates of the [CII] luminosity from the B11 IR luminosity function and Spinoglio et al $L_i - L_{IR}$ relations with the theorized dark matter power spectrum. On large scales, the fact that the clustering amplitude of [CII] fluctuations is proportional to the mean [CII] intensity indicates the potential for measuring cosmic evolution of aggregate [CII] emission with the line intensity mapping approach. For the fiducial experiment considered in this paper, we have found that it would be possible to measure the [CII] luminosity density with fractional errors on the order of 10%. In examining the effect of luminosity function shape, telescope aperture, and fractional error (or instrument noise level) on the relative performances of intensity mapping to galaxy surveys, we have further demonstrated that, in the case where experiments with low fractional errors are not feasible, intensity mapping experiments always outperform galaxy redshift surveys when measuring the mean [CII] intensity, and, for steep luminosity functions, the clustering power spectrum, as well.

APPENDIX

To explore the effect of the luminosity function shape on the relative performances of intensity mapping and galaxy surveys in observing the [CII] power spectrum and mean intensity of [CII] emitters, we have introduced toy models to represent different $\Phi(L_{IR}, z) \equiv \frac{dN}{dL_{IR}dV}$.

We parametrize our luminosity function as a Schechter function

$$\Phi(L_{IR}, z)dL_{IR} = n_* \left(\frac{L_{IR}}{L_*} \right)^\alpha \exp \left(-\frac{L_{IR}}{L_*} \right) d \left(\frac{L_{IR}}{L_*} \right) \quad (1)$$

where n_* is the normalization for number density, L_* is the characteristic luminosity at the knee, and α is the faint-end slope, as usual.

Power-law luminosity functions are notoriously ill-behaved if the lower limit of integration for either the luminosity functions or its moments is extended to zero. Rather than implement a break in the power law, we simply cut it off at some $L_{IR,min}$ and choose to fix in our analysis the total IR luminosity density from galaxies as predicted by B11, denoted as ρ_{IR}^{B11} , such that

$$\int d \left(\frac{L_{IR}}{L_*} \right) n_* L_* \left(\frac{L_{IR}}{L_*} \right)^{\alpha+1} \exp \left(-\frac{L_{IR}}{L_*} \right) \equiv \rho_{IR}^{B11} \quad (2)$$

This is motivated by the observation that in many cases we do have constraints on the integrated light (from, for example, the cosmic infrared background or from the cosmic star formation rate density or the requirement of critical reionization), whereas we may not in general have detailed constraints on the distribution of light among galaxies, i.e., the shape of luminosity function.

The number density of sources, n , can, in turn, be computed from

$$n = \int d \left(\frac{L_{IR}}{L_*} \right) n_* \left(\frac{L_{IR}}{L_*} \right)^\alpha \exp \left(-\frac{L_{IR}}{L_*} \right) \quad (3)$$

Finally, equation 2 allows us to calculate the [CII] luminosity density for each IR-normalized toy model as

$$\rho_{[CII]} = \int d \left(\frac{L_{IR}}{L_*} \right) n_* L_* \left(\frac{L_{IR}}{L_*} \right)^\alpha f_{[CII]} L_{IR} \exp \left(-\frac{L_{IR}}{L_*} \right) \quad (4)$$

where $f_{[\text{CII}]}$ is the fraction of IR luminosity emitted in [CII], or $\frac{L_{[\text{CII}]}(L_{\text{IR}})}{L_{\text{IR}}}$, described by the Spinoglio relations. Because $L_{[\text{CII}]}$ is slightly sublinear in L_{IR} , it follows that the toy models with steep faint-end slopes will produce more [CII] emission than their flatter counterparts.

REFERENCES

- B  thermin, M., Dole, H., Lagache, G., Le Borgne, D., & Penin, A. 2011, *A&A*, 529, A4
- Bouwens, R. J. et al. 2014, ArXiv e-prints
- Brauher, J. R., Dale, D. A., & Helou, G. 2008, *ApJS*, 178, 280
- Burgarella, D. et al. 2013, *A&A*, 554, A70
- Casey, C. M., Narayanan, D., & Cooray, A. 2014, ArXiv e-prints
- Chang, T.-C., Pen, U.-L., Bandura, K., & Peterson, J. B. 2010, ArXiv e-prints 1007.3709
- Cooray, A. et al. 2010, *A&A*, 518, L22
- de Putter, R., Holder, G. P., Chang, T.-C., & Dore, O. 2014, ArXiv e-prints
- D  az-Santos, T. et al. 2013, *ApJ*, 774, 68
- Dole, H. et al. 2006, *A&A*, 451, 417
- Glenn, J. et al. 2010, *MNRAS*, 409, 109
- Gong, Y., Cooray, A., Silva, M., Santos, M. G., Bock, J., Bradford, C. M., & Zemcov, M. 2012, *ApJ*, 745, 49
- Gong, Y., Cooray, A., Silva, M. B., Santos, M. G., & Lubin, P. 2011, *ApJ*, 728, L46
- Graci  -Carpio, J. et al. 2011, *ApJ*, 728, L7
- Hopkins, A. M. & Beacom, J. F. 2006, *ApJ*, 651, 142
- Jullo, E. et al. 2012, *ApJ*, 750, 37
- Kennicutt, Jr., R. C. 1998, *ApJ*, 498, 541
- Lidz, A., Furlanetto, S. R., Oh, S. P., Aguirre, J., Chang, T.-C., Dor  , O., & Pritchard, J. R. 2011, *ApJ*, 741, 70
- Morales, M. F. & Wyithe, J. S. B. 2010, *ARA&A*, 48, 127
- Parsons, A. R. et al. 2013, ArXiv e-prints 1304.4991
- Planck Collaboration et al. 2013, ArXiv e-prints
- Pullen, A., Dore, O., & Bock, J. 2013, ArXiv e-prints
- Sargsyan, L. et al. 2012, *ApJ*, 755, 171
- Smith, R. E. et al. 2003, *MNRAS*, 341, 1311
- Spinoglio, L., Dasyra, K. M., Franceschini, A., Gruppioni, C., Valiante, E., & Isaak, K. 2012, *ApJ*, 745, 171
- Switzer, E. R. et al. 2013, *MNRAS*, 434, L46
- Tingay, S. J. et al. 2013, *Journal of Physics Conference Series*, 440, 012033
- Viero, M. P. et al. 2012, ArXiv e-prints
- Visbal, E. & Loeb, A. 2010, *J. Cosmology Astropart. Phys.*, 11, 16
- Visbal, E., Trac, H., & Loeb, A. 2011, *J. Cosmology Astropart. Phys.*, 8, 10